

High Interfacial-Energy Interphase Promoting Safe Lithium Metal Batteries

Sufu Liu, Xiao Ji, Jie Yue, Singyuk Hou, Pengfei Wang, Chunyu Cui, Ji Chen, Bowen Shao, Jingru Li, Fudong Han,* Jiangping Tu,* and Chunsheng Wang*



Cite This: *J. Am. Chem. Soc.* 2020, 142, 2438–2447



Read Online

ACCESS |



Metrics & More

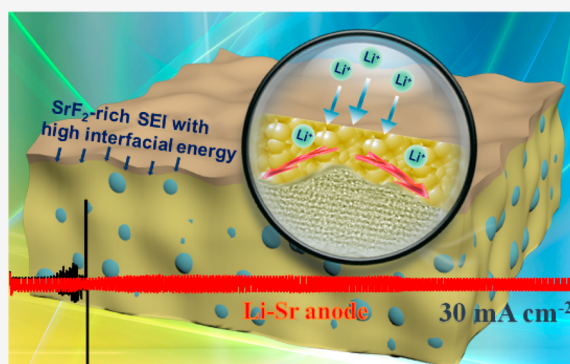


Article Recommendations



Supporting Information

ABSTRACT: Engineering a stable solid electrolyte interphase (SEI) is critical for suppression of lithium dendrites. However, the formation of a desired SEI by formulating electrolyte composition is very difficult due to complex electrochemical reduction reactions. Here, instead of trial-and-error of electrolyte composition, we design a Li-11 wt % Sr alloy anode to form a SrF_2 -rich SEI in fluorinated electrolytes. Density functional theory (DFT) calculation and experimental characterization demonstrate that a SrF_2 -rich SEI has a large interfacial energy with Li metal and a high mechanical strength, which can effectively suppress the Li dendrite growth by simultaneously promoting the lateral growth of deposited Li metal and the SEI stability. The Li–Sr/Cu cells in 2 M LiFSI-DME show an outstanding Li plating/stripping Coulombic efficiency of 99.42% at 1 mA cm^{-2} with a capacity of 1 mAh cm^{-2} and 98.95% at 3 mA cm^{-2} with a capacity of 2 mAh cm^{-2} , respectively. The symmetric Li–Sr/Li–Sr cells also achieve a stable electrochemical performance of 180 cycles at an extremely high current density of 30 mA cm^{-2} with a capacity of 1 mAh cm^{-2} . When paired with LiFePO_4 (LFP) and $\text{LiNi}_{0.8}\text{Co}_{0.1}\text{Mn}_{0.1}\text{O}_2$ (NCM811) cathodes, Li–Sr/LFP cells in 2 M LiFSI-DME electrolytes and Li–Sr/NCM811 cells in 1 M LiPF_6 in FEC:FEMC:HFE electrolytes also maintain excellent capacity retention. Designing SEIs by regulating Li-metal anode composition opens up a new and rational avenue to suppress Li dendrites.



INTRODUCTION

The energy density of lithium-ion batteries (LIBs) is approaching its physicochemical limit, which stimulates research interests in next-generation energy storage systems beyond Li-ion chemistry.^{1–5} Li metal is widely regarded as the most promising anode due to it having the highest specific capacities (3860 mAh g^{-1}), the lowest redox potential (−3.04 V versus standard hydrogen electrode (SHE)), and the potential to be coupled with high-energy non-Li-containing cathodes such as S and O_2 .^{6–10} However, the implementation of rechargeable Li-metal batteries (LMBs) is actually a Gordian knot that has not been untied for decades.^{11–13}

One critical challenge of LMBs is the mossy and dendritic Li growth that results in a low Coulombic efficiency and electrolyte “dry-out” due to the continuous side reactions between metallic lithium and liquid electrolytes. The Li-dendrite growth can lead to early failure and even cell shorting with fire.^{14–16} Engineering a solid electrolyte interphase (SEI), a passivating layer formed on the Li-anode surface due to electrolyte decomposition, can effectively suppress the Li dendrite.^{17–19} Extensive efforts have been devoted to suppress Li dendrite by forming a robust SEI through manipulating the composition of the electrolytes, including sacrificial electrolyte additives,^{20–22} highly concentrated lithium salt,^{23–25} and fluorinated electrolytes.^{26,27} The

high Li plating/stripping Coulombic efficiency of >99% was achieved only at a small current (<1 mA cm^{-2}), presumably due to the difficulties of suppressing dendrite growth at high currents.^{28,29} The key reason for the limited success in dendrite suppression is that most of the previous efforts attempt to build a mechanically robust SEI to suppress the Li-dendrite growth,^{30–32} while the interface nature at Li/SEI does not change. When the interface energy at SEI/Li is low and the mechanical strength of the SEI is not strong enough, the Li dendrite will penetrate through the SEI due to the large volume change during Li plating/stripping (Figure 1a).^{33,34}

We reported that a combination of Li/SEI interface energy (γ) and Young's modulus (E) of the SEI controls the Li-dendrite formation and growth.³⁵ γE has been used as a criterion to evaluate the Li-dendrite suppression ability. A high interfacial energy (γ) of the SEI can improve the mobility of Li atoms along the interphase and suppress Li penetration into SEI due to the high-energy penalty which suppresses the vertical, dendritic

Received: November 6, 2019

Published: January 13, 2020



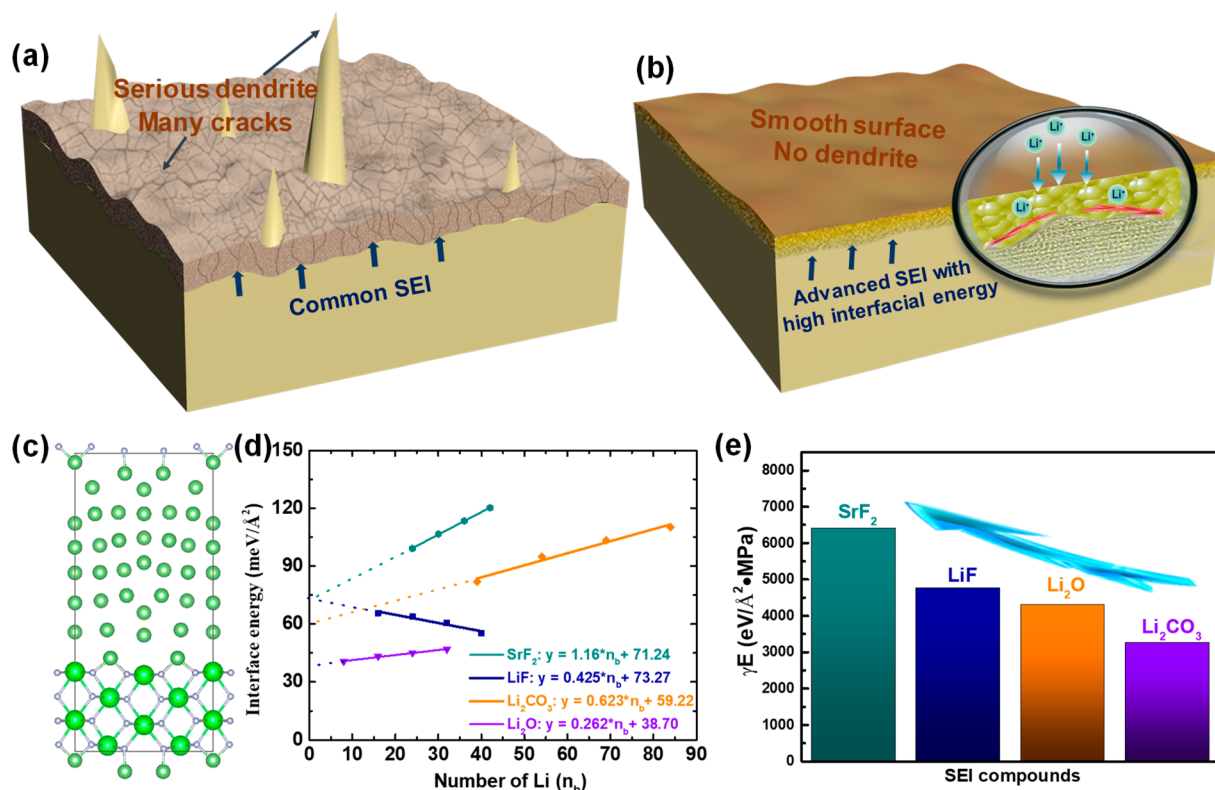


Figure 1. Schematic mechanism and DFT calculations for the high-interfacial-energy interphase on suppressing Li dendrite. Schematic diagram comparison of (a) serious dendrite formation in the conventional Li-metal anode with unprotected layer and (b) enhanced Li mobility along the interphase and uniform Li deposition in an advanced Li-metal anode with high interfacial energy. (c) Atomic structure of the SrF_2/Li interface and (d) the calculated interface energy γ of various possible SEI components versus the number of Li-metal formula units by DFT calculations. (e) The summary of Li-dendrite suppression ability γE for different SEI compounds.

growth of Li (Figure 1b).^{35,36} Theoretical calculation suggested that LiF has the highest γE value in all Li compounds formed in SEI due to the high interfacial energy at LiF/Li and high Young's modulus (E) of LiF. LiF-rich SEIs have been used to suppress the formation of dendrites in both liquid and solid electrolytes, validating the effectiveness of the approach.^{37,38} However, the critical current for Li cycling is still less than 10 mA cm^{-2} in all reported electrolytes, limiting the energy density and power density of Li-metal batteries. To further enhance the critical current and capacity, other metal fluoride SEIs that have higher γE to Li metal than that of LiF should be explored.

By screening the metal fluorides using density functional theory (DFT), we identified that SrF_2 has a higher γE value than LiF. Therefore, the SrF_2 SEI should more effectively suppress the Li dendrite. In this study, we successfully formed a SrF_2 -rich SEI on Li-11 wt % Sr alloy anodes in 2 M LiFSI-DME electrolytes. The higher Sr content in Li–Sr will increase the Li plating/stripping resistance due to the excess formation of SrF_2 with high interface energy with Li. The high reducing capability of Li–Sr enables the effective formation of the SrF_2 -rich interphase when immersed in fluorine-containing electrolyte. As a result, the Li-11 wt % Sr alloy anode achieves a high Li plating/stripping Coulombic efficiency up to 99.42% and shows a stable cycling performance at extremely high current of 30 mA cm^{-2} . The critical role of interface energy in dendrite suppression will also facilitate the development of next-generation rechargeable lithium-metal batteries.

RESULTS AND DISCUSSION

Synthesis and Characterization of the Li–Sr Anode.

Interfacial energy between Li and four inorganic SEI components (SrF_2 , LiF, Li_2O , and Li_2CO_3) was calculated using DFT (Figure 1c,d). The summary of Young's modulus and the calculated Li-dendrite suppression ability (γE) of these compounds are displayed in the table in Figure S1 and Figure 1e. Among these three traditional inorganic SEI components, LiF is proven to possess much higher γE of $4761 \text{ eV}/\text{\AA}^2 \text{ MPa}$ than Li_2O and Li_2CO_3 , showing the fluorinated interphase has the most outstanding dendrite suppression ability. However, the γE value ($6405 \text{ eV}/\text{\AA}^2 \text{ MPa}$) of SrF_2 is even higher than that ($4761 \text{ eV}/\text{\AA}^2 \text{ MPa}$) of LiF (Figure 1e) due to the high interfacial energy of $71.24 \text{ meV}/\text{\AA}^2$ against Li and a large Young's modulus of 89.91 GPa . Therefore, the SrF_2 -rich SEI formed on the Li surface could have a higher dendrite suppression ability than the LiF-rich SEI.

In order to form an intimate SrF_2 -rich SEI, the Li–Sr alloy was synthesized by heating and stirring the Li and Sr metal at 400°C in an Ar-filled glovebox. The schematic diagram (Figure 2a) illustrates the main strategy to fabricate the Sr–Li-metal alloys with the designed Li-11 wt % Sr composition. The mechanical stirring adopted in the alloying process is mainly to enhance the homogeneity of the final Li-11 wt % Sr alloys. According to the phase diagram (Figure S2), the cooling of Li-11 wt % Sr liquid (the atomic ratio of Sr is 1.0%) shown with the dashed line (M line) experiences sequence phase changes. At the temperature of 400°C , Li-11 wt % Sr is above its liquidus, and the mixture is in an all-liquid state (Figure S3). When the Li-11 wt % Sr liquid cooled to liquidus temperature (around 200°C), Li metal starts

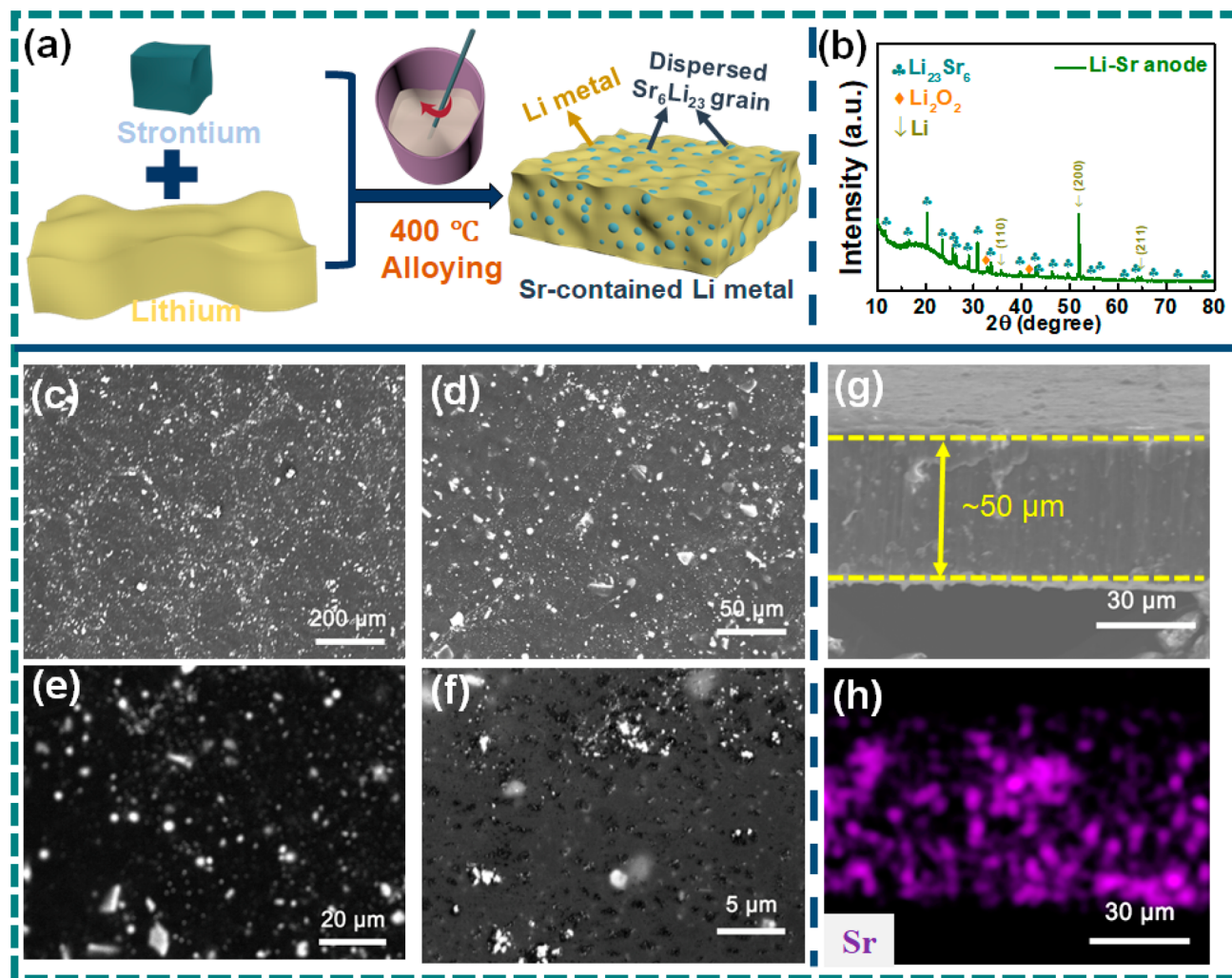


Figure 2. Fabrication and characterization of the Li–Sr anode. (a) The schematic diagram for the fabrication of the Li–Sr anode and (b) XRD pattern of the as-prepared Li–Sr anode. The corresponding (c and d) SEM and (e and f) backscattered electron images of the Li–Sr anode. (g) Cross-sectional photography of the Li–Sr anode after the rolling process and (h) the elemental mapping of Sr to confirm the homogeneous distribution of $\text{Sr}_6\text{Li}_{23}$.

to precipitate out of the liquid. As the temperature is further decreased to the eutectic point (135.7°C), the liquid crystallizes to form crystals of $\text{Sr}_6\text{Li}_{23}$ and solid Li metal. After all the liquid is consumed, only solid $\text{Sr}_6\text{Li}_{23}$ and Li-metal remain, and the content of pure Li metal in the final product is 82.25 wt % (93.5% in volume) based on the Lever rule.

The structure and morphology of the Li–Sr alloys were characterized using X-ray diffraction (XRD) and scanning electron microscopy (SEM). All the peaks in the XRD of Li-11 wt % Sr in Figure 2b are indexed to Li and $\text{Sr}_6\text{Li}_{23}$, which is consistent with the phase diagram. The three distinguished peaks around 36.2 , 52.2 , and 65.3° correspond to (110), (200), and (211) of Li metal, respectively. The existence of Li_2O is due to oxidation of Li during the sample transfer process. A rolling process (Figure S4) is carried out to reduce the thickness and surface roughness. Figure S5a shows the photographic image of a thin Li–Sr foil. The thickness of rolled Li–Sr foil is around $50\ \mu\text{m}$ as demonstrated in the cross-section SEM image of rolled Li–Sr foil (Figure S5b). The $50\ \mu\text{m}$ Li–Sr foil has an excellent flexibility (Figure S5c). It should be noted that the bare Li foil contrast used here has a typical thickness as high as $200\ \mu\text{m}$ (Figure S6). The SEM images with different scale (Figure 2c,d) show that the $\text{Sr}_6\text{Li}_{23}$ phase (white spots) is uniformly dispersed

in the Li matrix. The energy-dispersive spectroscopy (EDS) confirmed that white spots are the $\text{Sr}_6\text{Li}_{23}$ phase (Figure S7a,b). The backscattered electron images, which are an effective tool to detect the contrast between areas with different chemical compositions, are also captured. Since Sr is a much heavier element than Li (with a lower atomic number), backscattered electrons of Sr are stronger, and thus the Sr-enriched area appears brighter in the image (Figure 2e,f). The homogeneous distribution of the $\text{Sr}_6\text{Li}_{23}$ phase in the Li matrix can also be revealed in the cross-section (Figure 2g,h) and external (Figure S7c,d) EDS mapping of the Li–Sr film.

Formation and Stability of a SrF_2 -Rich SEI in Fluorinated Electrolytes. A SEI will be formed on the surface of the Li–Sr electrode in 2 M LiFSI-DME electrolytes as schematically demonstrated in Figure 3a. As shown in Figure S8a, a distinct surface layer is homogeneously formed on the Li–Sr electrode after immersion in the 2 M LiFSI-DME electrolyte overnight. The aerial view (Figure S8b and c) reveals $\text{Sr}_6\text{Li}_{23}$ nanoparticles are clearly wrapped in the coating. The structure of the SEI was further characterized via scanning transmission electron microscopy (STEM). As shown by the selected area electron diffraction (SAED) image in Figure S9a, the SEI displays a polycrystalline nature of inorganic nanoparticles. The

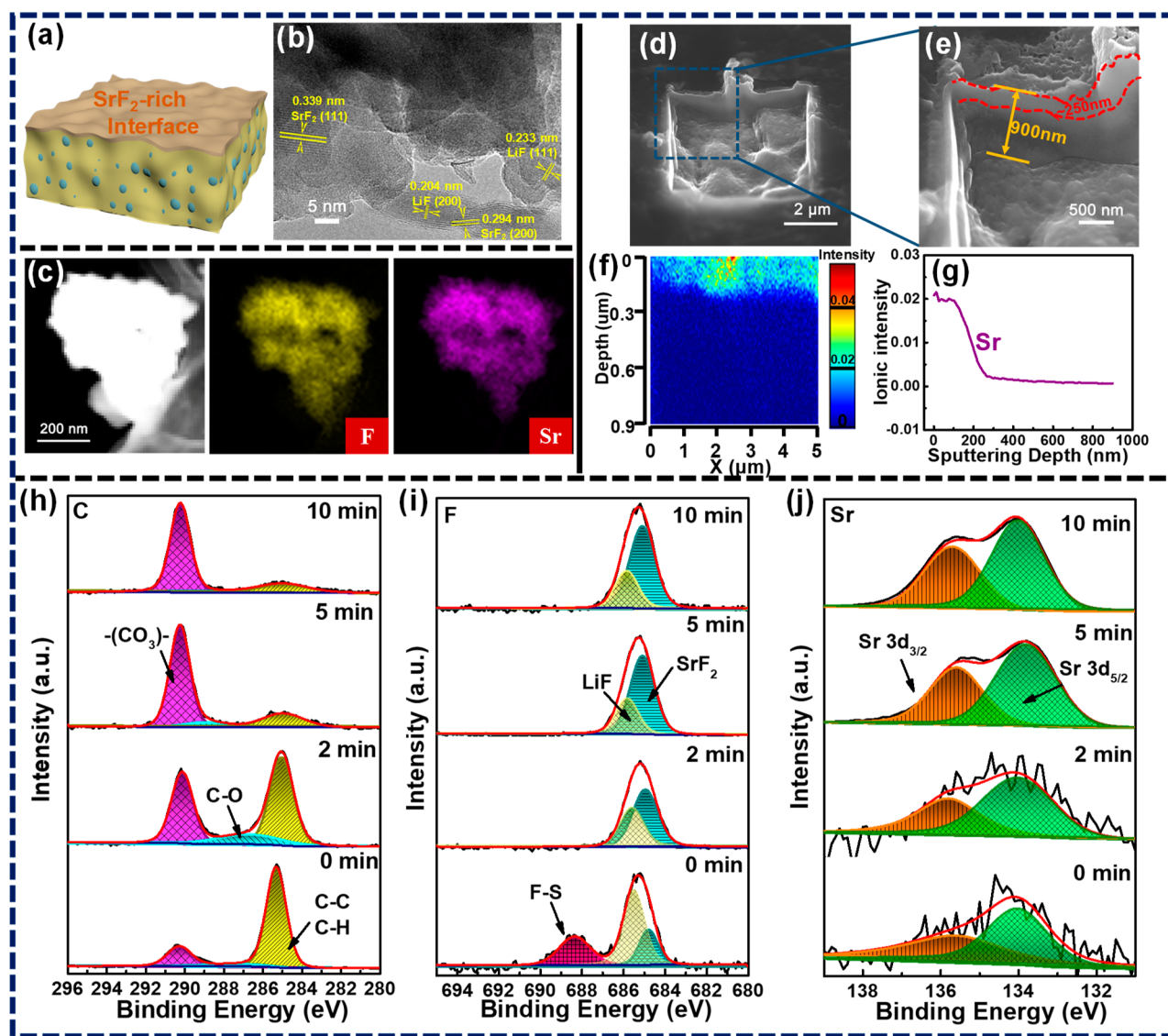


Figure 3. Surface characterizations of the Li–Sr anode after immersion in fluorinated electrolyte. (a) The schematic figure revealing that the SrF_2 -rich interphase is formed on the Li–Sr anode surface after immersion in fluorine-containing electrolyte. (b) The high-resolution TEM images of the SEI of the Li–Sr anode and (c) the corresponding EDS elemental mapping images of Sr, F. (d–g) TOF-SIMS analysis of the interface: (d) The crater sputtered by a Ga^+ ion beam and (e) a magnified interface, (f) TOF-SIMS analysis for the Sr element, and (g) Sr element distribution of the cross-sectional surface. (h–j) In-depth XPS spectra of the resulting SEI formed on the Li–Sr anode: C 1s spectra (h), F 1s spectra (i), and Sr 3d spectra (j).

magnified high-resolution TEM image in Figure 3b shows distinct lattice fringes of the crystalline region and amorphous areas of the organic polymer in the SEI. The lattices with plane spacing of 0.339 and 0.294 nm correspond to the (111) and (200) lattice planes of SrF_2 , respectively. The other two sets of lattices with lattice spacing of 0.204 and 0.233 nm can be ascribed to LiF (200) and (111) lattice planes, respectively. In addition, a large lattice fringe of 0.522 nm is also observed, corresponding to the (220) lattice planes of residual $\text{Sr}_6\text{Li}_{23}$ (Figure S9b). Moreover, a uniform elemental distribution of F and Sr on the SEI layer is also revealed in the elemental mapping images (Figure 3c), which further confirms the spontaneous reaction between the Li–Sr anode and 2 M LiFSI-DME electrolytes. This is mainly attributed to the reduction of LiFSI salt. LiFSI salt has a much lower unoccupied molecular orbital energy (−1.70 eV) than that of the DME (1.6 eV). Therefore, LiFSI has a higher tendency to be reduced, and the S–F bond in the $-\text{SO}_2\text{F}$ group will be first broken to provide a fluorine

source, resulting in the fluoride being in the final SEI of the Li–Sr electrode. Notice that the potentials of both Li metal (−3.04 V) and Sr metal (−2.89 V) are below the reduction potentials of 2 M LiFSI-DME electrolyte, so both Li and Sr will lose electrons simultaneously and combine with a dissociative fluorine ion to form the LiF and SrF_2 in the interphase.

Time-of-flight secondary ion mass spectroscopy (TOF-SIMS) was used to determine the thickness of the SrF_2 -rich layer on the Li–Sr anode surface. As shown in Figure 3d–g, the surface of the Li–Sr anode after immersion in 2 M LiFSI for 12 h is carved and analyzed by ion beam over a $5 \mu\text{m} \times \mu\text{m}$ area. A large amount of Sr can be found within the top surface layer (Figure 3f), and the depth of Sr is determined to be around 250 nm (Figure 3g). This is consistent with the cross-section view revealed in Figure 3e; i.e., a surface layer around 250 nm with different depth of field from below can be clearly found. Meanwhile, in the negative ion mode, a strong F signal can also

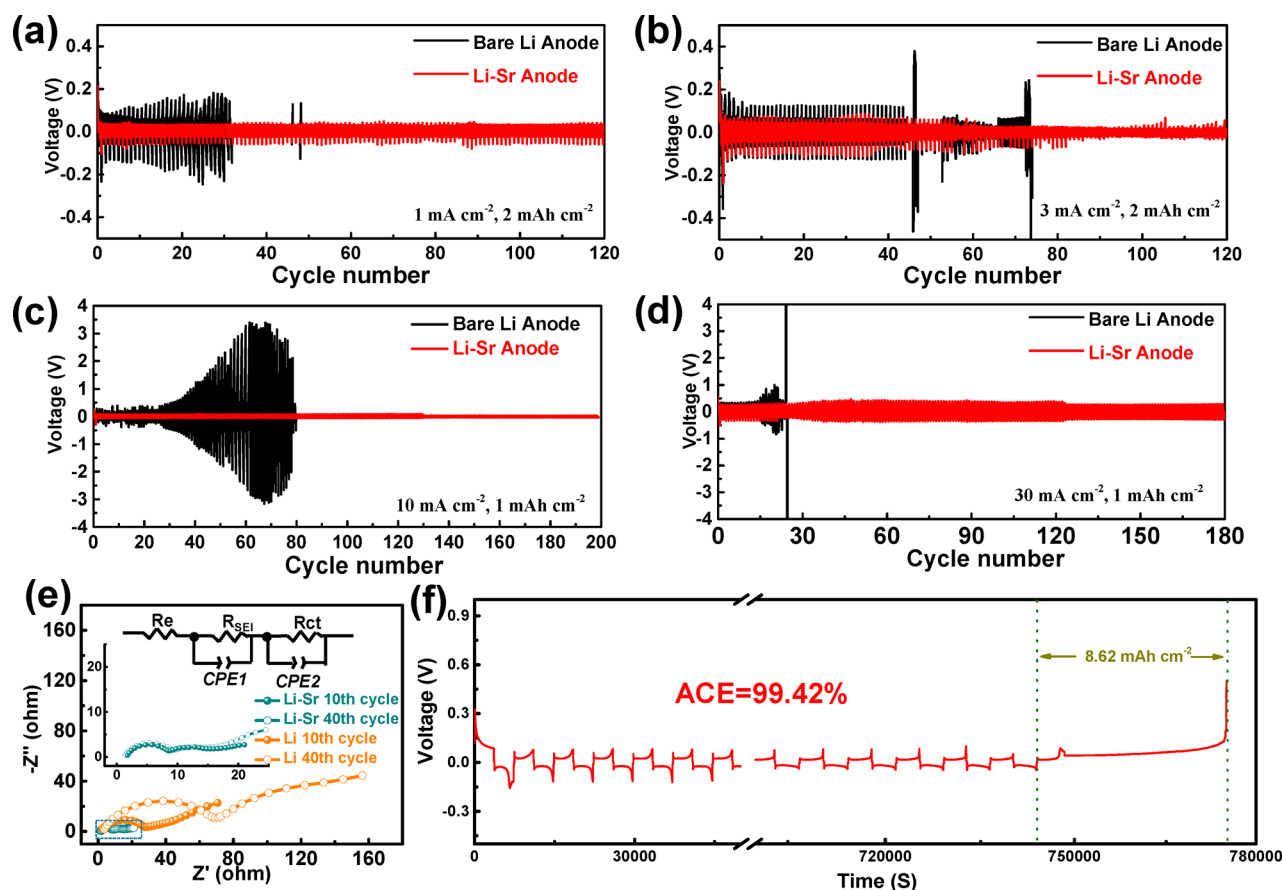


Figure 4. Electrochemical performance of bare Li and Li-Sr anodes in symmetrical cells. (a–d) Galvanostatic discharge/charge voltage profiles of bare Li and Li-Sr electrodes in symmetric coin cells at (a) 1 mA cm⁻² and (b) 3 mA cm⁻² with a stripping/plating capacity of 2 mAh cm⁻² and at (c) 10 mA cm⁻² and (d) 30 mA cm⁻² with a stripping/plating capacity of 1 mAh cm⁻². (e) Impedance plots of the symmetric cells after 10 and 40 cycles at 10 mA cm⁻². (f) The average Li plating/stripping Coulombic efficiency in the Li-Sr/Li-Sr cell in the 100 cycles at 1 mA cm⁻² with a capacity of 1 mAh cm⁻² using the special method described in Figure S17.

be found on the surface layer (Figure S10), which is consistent with the Sr distribution.

The chemical compositions of the interphase formed on the Li-Sr anode were also analyzed using in-depth X-ray photoelectron spectroscopy (XPS) by continuous Ar ion etching. Typically, the organic hydrocarbon species are mainly distributed at the surface region, and their signal gradually decreases after sputtering. In contrast, the content of the inorganic components (such as LiF and Li₂CO₃), which has higher binding energies with Li, increases from the surface to the internal closing to Li. The C 1s spectra (Figure 3h) indicate that the organic ingredients are composed of three main parts, including the carbonate group (~290.0 eV, -(CO₃)-), carbonic oxide (~287 eV, C-O), and hydrocarbon (~285.0 eV, C-C and C-H). Figure 3i presents the high-resolution spectra of F 1s. The peak positions of LiF (684.9 eV) and SrF₂ (684.5 eV) are very close due to their similar binding energy. With subsequent etching, the content of F-S (688.4 eV) in the SEI disappears after 120 s sputtering, while the signal of SrF₂ rises sharply and abundant LiF still exists, which is contributed by the reduction of FSF⁻. To further confirm the existence of SrF₂, the combination of F 1s and Sr 3d spectra should be considered. From the Sr 3d spectra (Figure 3j), the peaks located at 135.8 and 134.0 eV are assigned to Sr 3d_{5/2} and Sr 3d_{3/2}, respectively. This is consistent with the state of Sr²⁺, which has a binding energy separation between the core levels around

1.8 eV. Meanwhile, the enhanced SrF₂ signal is also consistent with the result in Figure 3i. Therefore, a SrF₂-rich interphase is formed on the surface Li-Sr electrode.

It needs to be emphasized that the great dendrite suppression capability of the Li-Sr anode is due to the SrF₂-rich interphase (not the Li-Sr material) which can be formed as soon as the anode is soaked in the fluorinated electrolyte (as shown in Figure 3) and will always be present on the surface at different states of charges (SOCs) (Figure S11 and Figure S12). Due to its low electronic conductivity and high interfacial energy with Li metal, the SrF₂-rich layer functions as a SEI, promoting the smooth Li deposition underneath it and suppressing dendrite formation.

Electrochemical Performance of the Li-Sr Anode in Symmetrical Cells. The delithiation behavior and capacity of an ultrathin 50 μm Li-Sr anode were also elucidated by assembling a Li-Sr||Cu cell. At a current density of 0.5 mA cm⁻² with a cutoff voltage of 0.5 V, the ultrathin Li-Sr electrode can deliver an area capacity of 9.2 mAh cm⁻² (Figure S13a) and gravity capacity of 3410 mAh g⁻¹ (of the mass of the whole electrode). During the delithiation (Li stripping) process, Li metal in the Li-Sr anode is first stripped at an overpotential around 0.05 V because the delithiation potential of Sr₆Li₂₃ is higher than the stripping potential of pure Li metal. When the Li stripping capacity reaches 8.8 mAh cm⁻², the Sr₆Li₂₃ begins to delithiate. Ex-situ XRD is conducted to further verify the

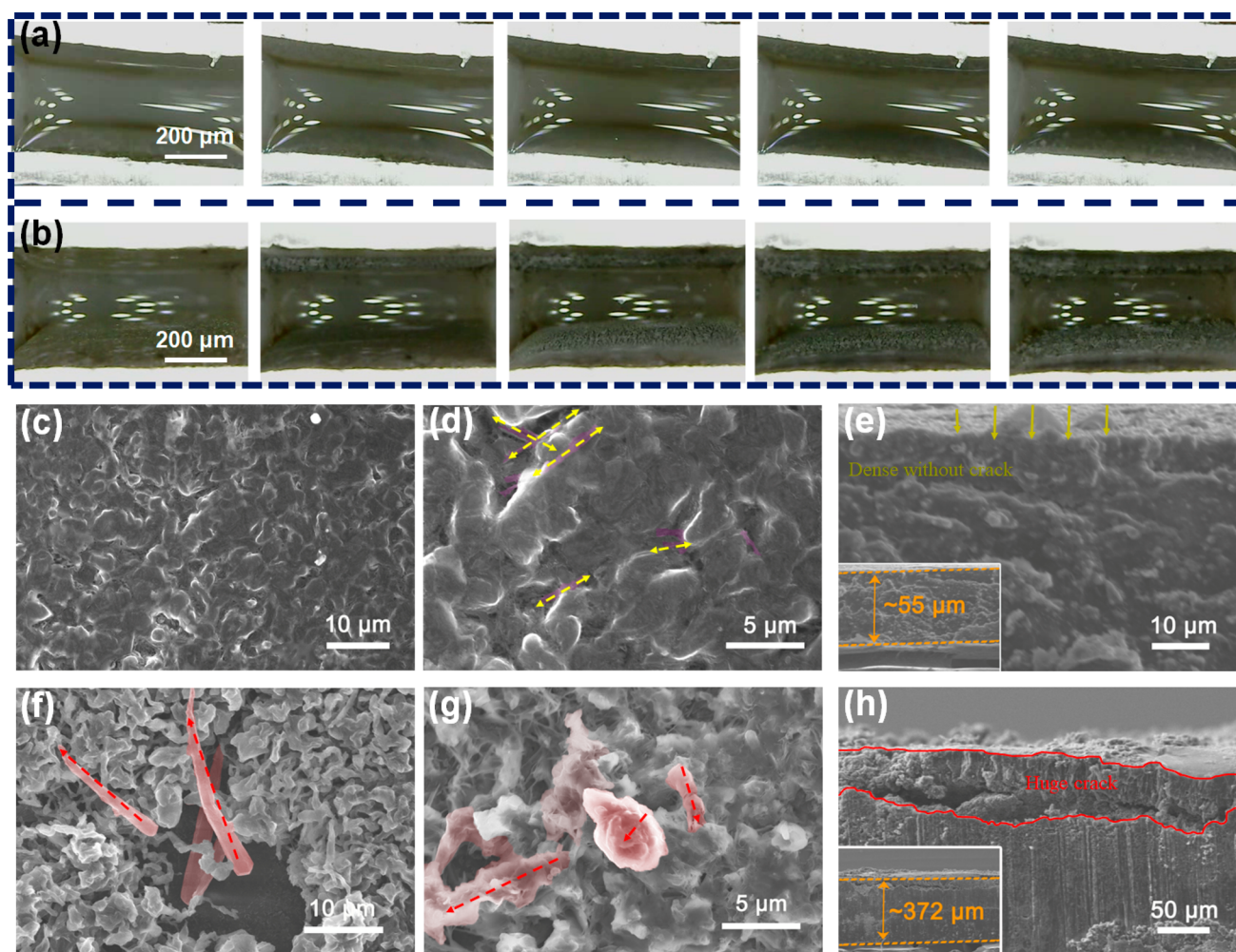


Figure 5. Dendrite comparison of different anodes after cycling. In situ optical microscopy observations (captured from the [Movie S1](#) and [S2](#)) of the electrolyte–electrode interface during electrodeposition on the (a) Li–Sr and (b) Li electrodes for two cycles at 3 mA cm^{-2} with a capacity of 0.25 mAh cm^{-2} (play speed is set by 10 times). Comparison of top-view and cross-sectional SEM images of (c–e) Li–Sr and (f–h) bare Li anode after 20 cycles at 10 mA cm^{-2} .

delithiation process. As demonstrated in [Figure S13b](#), during the initial discharging process to 5 mAh cm^{-2} , the peaks associated with the phase of $\text{Sr}_6\text{Li}_{23}$ maintain unchanged, while the characteristic peaks of Li at around 36.2 and 52.0 degrees, corresponding to the (110) and (200) faces of metal Li, respectively, gradually disappear. Upon further delithiation to 8 mAh cm^{-2} , the content of Li further decreases, while the peaks of $\text{Sr}_6\text{Li}_{23}$ are still maintained, confirming that Li metal is stripped prior to the delithiation of $\text{Sr}_6\text{Li}_{23}$. This can also be supported by the continuous increase of Li peaks on the XRD result of the Cu electrode during discharge ([Figure S13c](#)). However, no signal of Sr and $\text{Sr}_6\text{Li}_{23}$ can be found in plated Li on Cu although the discharging voltage has reached 0.5 V . Hence, Sr mainly plays a role in forming the SrF_2 -rich interphase layer and will not participate in the plating/stripping process, and therefore our Li–Sr anode is fundamentally different from other alloy anodes like Li–Na³⁹ and Na–K.⁴⁰

To validate the role of a SrF_2 -rich SEI in Li stripping/plating, we compared the performances of symmetric Li–Sr/Li–Sr cells with Li–Li cells. [Figure 4a–d](#) shows the specific voltage profiles as a function of cycle number at various current densities and capacities. The symmetric batteries were first evaluated at a fixed capacity of 2 mAh cm^{-2} but at different currents ([Figure 4a](#) and

[b](#)). The Li–Sr/Li–Sr cell exhibits a very stable voltage profile at a current of 1 mA cm^{-2} compared to the one with Li metal (15 versus 60 mV at the 20th cycle). When the current density is increased to 3 mA cm^{-2} , the voltage of bare Li metal after 40 cycles begins to fluctuate violently, and the overpotential occasionally reaches 400 mV . [Figure S14](#) displays the specific cycling profiles between the 50th and 60th cycles. A sudden voltage drop happens at the 53th cycle for the bare Li metal, followed with random voltage oscillation and large overpotential at a later stage. However, the composite Li–Sr anodes exhibit a much lower average voltage hysteresis of less than 40 mV throughout the whole 120 cycles, indicating the excellent stability of Li plating/stripping under a SrF_2 -rich SEI.

The electrochemical performances of the symmetrical Li/Li and Li–Sr/Li–Sr cells are also compared under a low areal capacity of 1 mAh cm^{-2} but at a much larger current density up to 30 mA cm^{-2} . As shown in [Figure S15a](#), the Li–Sr/Li–Sr symmetrical cell at a low current of 1 mA cm^{-2} can maintain a stable discharging/charging process for more than 280 cycles, while the voltage profile of the Li/Li cell is only stabilized in the first 56 cycles. Its overpotential shows irregular rises and falls in the range of 23 – 148 mV subsequently, indicating the failure of the cell. When the symmetrical Li/Li and Li–Sr/Li–Sr cells

were cycled at a high value of 10 mA cm^{-2} with a capacity of 1 mAh cm^{-2} (Figure 4c), the Li/Li cell shows increased polarization after 20 cycles due to the rapid increase in the SEI layer by the repeated cracking/reforming cycles. The low interface energy and strong bonding between SEI and Li induce SEI cracks during a large volume change of Li at a high current. The new SEI will form at cracks causing continuous SEI growth and increases in overpotential. In sharp contrast, the Li–Sr/Li–Sr cell delivers a stable overpotential around 60 mV without dramatic fluctuation during the whole 200 cycles. Carefully examining the Li plating/stripping overpotential between the 77th and 81st cycles of the Li–Sr/Li–Sr (Figure S16a) and Li/Li (Figure S16b) cells, the overpotential of the Li/Li cell abruptly drops to nearly 0 mV after a huge overpotential increase, indicating an internal short circuit of the Li/Li cell induced by the Li dendrites, while the Li–Sr/Li–Sr cell maintains stable overpotential without sharp fluctuations. A similar result is also found in the overpotential comparison of two cells at a high current of 15 mA cm^{-2} (Figure S15b), where Li–Sr/Li–Sr symmetric cells work normally with stable and low voltage plateaus for more than 190 cycles. In particular, when the current density is increased to an extremely high value of 30 mA cm^{-2} (Figure 4d), the Li/Li-metal cell can only be plated/stripped for 25 cycles before the short circuit, while the Li–Sr/Li–Sr cell can be cycled for more than 180 times, a nearly 7-fold improvement in cycling life. It should be mentioned that 30 mA cm^{-2} is an unprecedented high current density that has rarely been tested. Such a great difference effectively confirms the importance of the SrF_2 layer in stabilizing lithium electrodeposition.

Nyquist plots of symmetric cells were also performed to probe the interfacial impedance in the 10th and 40th cycling at 10 mA cm^{-2} (Figure 4e). The semicircle at high-frequency regions in the Nyquist plots corresponds to the SEI (denoted as R_{SEI}). The R_{SEI} of the Li–Sr/Li–Sr cell maintains a consistent value around 8.4Ω during the 10th to 40th cycle process. By contrast, the R_{SEI} of the Li/Li cell possesses a much larger change from 24Ω to nearly 70Ω . This can be attributed to the incompact native SEI and the uncontrollable dendrites, which give rise to the accumulated SEI layer with increased ionic resistance. To further prove the superiority SrF_2 -rich interphase layer, the average Coulombic efficiency (ACE) for Li plating/stripping in Li–Sr/Li–Sr cells is also calculated using a method described in Figure S17. As is shown in Figure 4f, a high ACE of 99.42% was obtained when cycled at 1.0 mA cm^{-2} with a capacity of 1 mAh cm^{-2} . In comparison, the simple coating of a SrF_2 microsphere layer on the polypropylene (PP) separator cannot suppress Li dendrite intrinsically.⁴¹ This is mainly because the directly obtained SrF_2 layer cannot generate an advanced SEI on the Li-metal surface with reforming capability. Due to the weak contact of SrF_2 microspheres with a separator as well as Li metal during cycling, the Li dendrite can still break through the unstable SEI separator and react with the electrolyte, reducing Coulombic efficiency as low as 80%. In addition, the Li dendrite can still grow through the pores among the SrF_2 –PP separator and cause short circuit eventually. Therefore, our designed Li–Sr anode provides a novel and distinct strategy to in situ integrate the SrF_2 -rich SEI of the Li-metal anode. The self-healing ability can always maintain the electrode interface with high interfacial energy, providing the potential for outstandingly electrochemical performance. Even when the capacity is increased to 2 mAh cm^{-2} at 3.0 mA cm^{-2} , the ACE can still maintain an outstanding value of 98.95% (Figure S18). The average Li

plating/stripping Coulombic efficiency (ACE) of Li–Sr anodes is one of the best in all reported Li anodes at similar currents and capacities.^{20,23,42}

Visualization of the Superior Dendrite Suppression Capability of the Li–Sr anode. To further illustrate the dendrite suppression capability of the SrF_2 -rich layer, we monitored the morphology of deposited Li by a combination of in situ optical microscopy and SEM. The optical microscopy is also compared (Figure 5a and b, captured from Movies S1 and S2, the speed is accelerated by 10 times) during the first two cycles of Li and Li–Sr anodes. In our case, both Li/Li and Li–Sr/Li–Sr symmetric cells were assembled in a sealed transparent case equipped with a digital camera. What needs to be mentioned is that because there is no conventional polymer separator or internal pressure in the optical cell it will facilitate the dendrite growth in comparison to the practical batteries under pressure. As visualized in Figure 5a, the Li–Sr electrode can still maintain a smooth surface without clear dendrite or pulverization. Despite that several protrusions start to appear after two cycles, the electrode is still very dense with no sign of severe dendrite formation. However, the protrusions are very pronounced along the edge for the Li-metal electrode, revealing the inhomogeneous Li deposition (Figure 5b). The mossy and dendritic Li with porous morphology becomes more predominant after two cycles, which exposes more fresh Li with high surface area to consume electrolyte and further aggravates Li-dendrite growth in the following depositions. These results vividly confirm the significant role of the SrF_2 layer in regulating Li electrodeposition behavior.

Figure 5c–h shows the SEM images of Li/Li and Li–Sr/Li–Sr cells after 20 cycles at 10 mA cm^{-2} with a stripping/plating capacity of 1 mAh cm^{-2} . Very different Li morphologies are observed on the Li–Sr and Li electrodes in both the top surface and cross section. As exhibited in Figure 5c, the top surface of the Li–Sr electrode stays smooth without an obvious Li dendrite. The bleached color of a fuzzy thin layer is attributed to the SEI formation. This is because the SEI always has a poor electron conductivity and therefore displays the sensitivity to the focused beam of electrons. When magnified (Figure 5d), there are also no sharp Li filaments to be found. The dashed lines in Figure 5d highlight some textures of Li-metal growth underneath the coverage, which seems only to coalesce and form a continuum in the horizontal plane. In addition, the volume change is also recorded by a cross-sectional view. As revealed in Figure 5e, the plated lithium under the SrF_2 -rich layer is very dense without any distinguished cracks, and the thickness is kept around $55 \mu\text{m}$, similar to the original thickness. This evidence verifies that the SrF_2 -rich layer is effective in suppressing Li-dendrite evolution in limited dimension over cycling. In contrast, localized Li deposition is clearly found for the Li metal (Figure 5f,g). Dendritic Li is loosely stacked after cycling, and needle-like dendrites with a diameter around $2 \mu\text{m}$ grow vertically toward the separator. A large amount of Li nanofilaments or protrusions are further confirmed in the enlarged view, and the uneven deposition with porous coverage will exacerbate reaction with the electrolyte, leading to the low CE during the repeated plating/stripping process. In addition, a huge shedding layer with a thickness around $50\text{--}80 \mu\text{m}$ is found on the surface layer of the Li electrode (Figure 5h), and the Li thickness increased to $270 \mu\text{m}$, forming porous Li due to the continuous corrosion of the surface and accumulation of dendritic or dead Li.

The morphology of the anodes after 80 cycles is also shown in Figure S19. The Li–Sr electrode remains flat in general despite some obvious wrinkles and grain particles (Figure S19a–c). On the contrary, the surface of Li metal is thoroughly corroded by huge cracks with serious pulverizations after 80 cycles at 10 mA cm⁻² (Figure S19d–f). The loosely connected structure with deleterious volume change is also revealed from the cross section, which further accelerates the rapid electrolyte corrosion and massive dendrite formation toward the separator, resulting in the short circuit as shown in Figure 4c. The cross-sectional image in Figure S20 further confirms the dense coverage of the SrF₂ coating, which effectively regulates the lateral Li-metal growth underneath and thus provides a strong guarantee for the long-term cycling.

Electrochemical Performance of the Li–Sr Anode in Full Cells. The electrochemical performance of Li–Sr and Li anodes is also compared in full cells by coupling with stable LiFePO₄ (LFP) cathodes. Li–Sr/LFP and Li/LFP full cells were evaluated in 2 M LiFSI-DME electrolytes at a high rate of 2 C (corresponding to a current density of 3.0 mA cm⁻²). Li/LFP full cells exhibit a sharply decreased capacity to a capacity of 21.6 mAh g⁻¹ after 110 cycles (Figure 6a). By contrast, Li–Sr/LFP

maintains a high capacity retention of 76.1% even after 100 cycles. Figure S21b and c exhibit the corresponding SEM images of Li–Sr anodes after 30 cycles at 1 C. There is also no overgrowth of Li filaments on the surface of the Li–Sr anode, which exhibits a uniform morphology and hence enables a high CE and utilization of Li metal as well. Therefore, these outstanding electrochemical performances further demonstrate the great potential of the Li–Sr anode as an advanced anode material for rechargeable Li-metal batteries.

CONCLUSIONS

In summary, we have demonstrated the critical role of SrF₂ in the SEI that has a high interface energy with Li in suppressing dendrite formation. By optimizing the structure of the Li-metal matrix with dispersive Sr₆Li₂₃ particles, a SrF₂-rich interphase can be generated when cycled in fluorine-rich electrolytes. TEM and XPS results reveal the agminated presence of nano-structured SrF₂ particles in the SEI of the Li–Sr anode. The SrF₂-rich Li–Sr anode enabled predominant lithium stripping/plating performance in a symmetric cell at an ultrahigh current density of 30 mA cm⁻² and improved the Coulombic efficiency up to 99.42%. Excellent capacity retention is also achieved in full cells of the Li–Sr anode with both LFP or NCM811 cathodes with practically relevant areal capacities (1.5 mAh cm⁻²). Such a design provides a new guidance to construct a high-interfacial-energy interphase to suppress dendrite formation. Our findings open up a new and promising strategy for rational optimization of advanced Li-metal anodes for the practical application of rechargeable Li-metal batteries.

ASSOCIATED CONTENT

Supporting Information

The Supporting Information is available free of charge at <https://pubs.acs.org/doi/10.1021/jacs.9b11750>.

Complete experimental details and additional data (PDF)

Movie S1 showing in situ optical microscopy observations of the bare Li-metal anode during cycling at 3 mA cm⁻² with a capacity of 0.25 mAh cm⁻² (MP4)

Movie S2 showing in situ optical microscopy observations of the Li–Sr anode during cycling at 3 mA cm⁻² with a capacity of 0.25 mAh cm⁻² (MP4)

AUTHOR INFORMATION

Corresponding Authors

Fudong Han – Department of Mechanical, Aerospace, and Nuclear Engineering, Rensselaer Polytechnic Institute, Troy, New York 12180, United States; orcid.org/0000-0003-2507-4340; Email: hanf2@rpi.edu

Jiangping Tu – State Key Laboratory of Silicon Materials, Key Laboratory of Advanced Materials and Applications for Batteries of Zhejiang Province, and School of Materials Science & Engineering, Zhejiang University, Hangzhou 310027, China; orcid.org/0000-0002-7928-1583; Email: tujp@zju.edu

Chunsheng Wang – Department of Chemical and Biomolecular Engineering, University of Maryland, College Park, Maryland 20740, United States; orcid.org/0000-0002-8626-6381; Email: cswang@umd.edu

Authors

Sufu Liu – Department of Chemical and Biomolecular Engineering, University of Maryland, College Park, Maryland 20740, United States; State Key Laboratory of Silicon Materials,

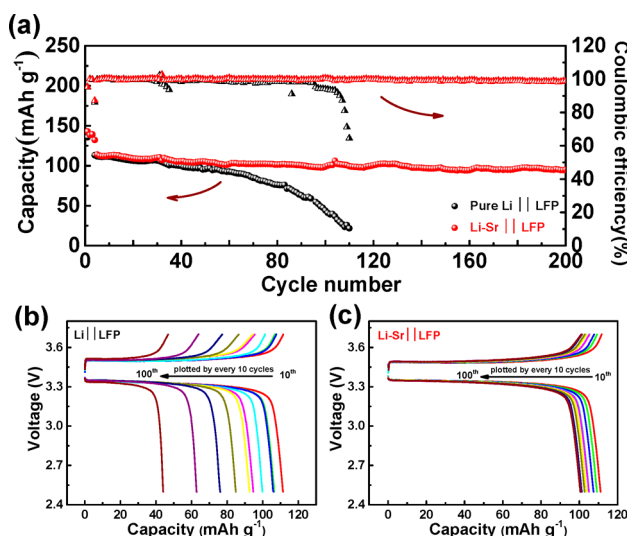


Figure 6. Full cell performance with different anodes. (a) Discharge capacity and Coulombic efficiency at 2 C and (b and c) typical discharge-charge curves at different cycles of the Li||LFP and Li–Sr||LFP cells (1 C = 170 mA g⁻¹ for LFP cathode).

cells deliver very stable capacity without huge fluctuation or degradation, and the capacity retains 95.3 mAh g⁻¹ after 200 cycles, nearly 84.3% of the original capacity. As shown in Figure 6b and c, the Li/LFP cell has a larger voltage hysteresis between the charge/discharge than Li–Sr/LFP. This can be attributed to the increasingly severe SEI passivation/pulverization of the bare lithium surface, which leads to a poor electrode kinetics with high impedance.

In order to further validate the effectiveness of the Li–Sr anodes, we also coupled Li–Sr anodes with high voltage LiNi_{0.8}Co_{0.1}Mn_{0.1}O₂ (NCM811) cathodes using a high voltage nonflammable all-fluorinated carbonate electrolyte (1 M LiPF₆ in FEC:FEMC:HFE). Outstanding performance is also achieved for a high voltage Li–Sr/NCM811 cell. As shown in Figure S21a, with identical electrochemical performances around 195 mAh g⁻¹ for the first cycle at 1 C, the Li–Sr/NCM811 cell

Key Laboratory of Advanced Materials and Applications for Batteries of Zhejiang Province, and School of Materials Science & Engineering, Zhejiang University, Hangzhou 310027, China

Xiao Ji – Department of Chemical and Biomolecular Engineering, University of Maryland, College Park, Maryland 20740, United States

Jie Yue – Department of Chemical and Biomolecular Engineering, University of Maryland, College Park, Maryland 20740, United States

Singyuk Hou – Department of Chemical and Biomolecular Engineering, University of Maryland, College Park, Maryland 20740, United States

Pengfei Wang – Department of Chemical and Biomolecular Engineering, University of Maryland, College Park, Maryland 20740, United States; orcid.org/0000-0001-9882-5059

Chunyu Cui – Department of Chemical and Biomolecular Engineering, University of Maryland, College Park, Maryland 20740, United States

Ji Chen – Department of Chemical and Biomolecular Engineering, University of Maryland, College Park, Maryland 20740, United States; orcid.org/0000-0003-0326-8304

Bowen Shao – Department of Mechanical, Aerospace, and Nuclear Engineering, Rensselaer Polytechnic Institute, Troy, New York 12180, United States

Jingru Li – State Key Laboratory of Silicon Materials, Key Laboratory of Advanced Materials and Applications for Batteries of Zhejiang Province, and School of Materials Science & Engineering, Zhejiang University, Hangzhou 310027, China

Complete contact information is available at:

<https://pubs.acs.org/10.1021/jacs.9b11750>

Notes

The authors declare no competing financial interest.

ACKNOWLEDGMENTS

This work was supported by the US Department of Energy (DOE) under award No. DEEE0008202. We acknowledge the University of Maryland supercomputing resources (<http://hpcc.umd.edu>) made available for conducting DFT computations in this paper. We also thank the Maryland NanoCenter and its AIMLab for characterization support.

REFERENCES

- (1) Duan, H.; Yin, Y. X.; Shi, Y.; Wang, P. F.; Zhang, X. D.; Yang, C. P.; Shi, J. L.; Wen, R.; Guo, Y. G.; Wan, L. J. Dendrite-Free Li-Metal Battery Enabled by a Thin Asymmetric Solid Electrolyte with Engineered Layers. *J. Am. Chem. Soc.* **2018**, *140* (1), 82–85.
- (2) Li, Y. Z.; Li, Y. B.; Pei, A. L.; Yan, K.; Sun, Y. M.; Wu, C. L.; Joubert, L. M.; Chin, R.; Koh, A. L.; Yu, Y.; Perrino, J.; Butz, B.; Chu, S.; Cui, Y. Atomic structure of sensitive battery materials and Interfaces revealed by cryo-electron microscopy. *Science* **2017**, *358* (6362), 506–510.
- (3) Harry, K. J.; Hallinan, D. T.; Parkinson, D. Y.; MacDowell, A. A.; Balsara, N. P. Detection of subsurface structures underneath dendrites formed on cycled lithium metal electrodes. *Nat. Mater.* **2014**, *13* (1), 69–73.
- (4) Wei, S.; Choudhury, S.; Tu, Z.; Zhang, K.; Archer, L. A. Electrochemical interphases for high-energy storage using reactive metal anodes. *Acc. Chem. Res.* **2018**, *51* (1), 80–88.
- (5) Cheng, X. B.; Zhang, R.; Zhao, C. Z.; Zhang, Q. Toward safe lithium metal anode in rechargeable batteries: a review. *Chem. Rev.* **2017**, *117* (15), 10403–10473.
- (6) Zeng, X. X.; Yin, Y. X.; Li, N. W.; Du, W. C.; Guo, Y. G.; Wan, L. J. Reshaping Lithium Plating/Stripping Behavior via Bifunctional

Polymer Electrolyte for Room-Temperature Solid Li Metal Batteries. *J. Am. Chem. Soc.* **2016**, *138* (49), 15825–15828.

(7) Choudhury, S.; Wan, C. T.; Al Sadat, W. I.; Tu, Z.; Lau, S.; Zachman, M. J.; Kourkoutis, L. F.; Archer, L. A. Designer interphases for the lithium-oxygen electrochemical cell. *Sci. Adv.* **2017**, *3* (4), No. e1602809.

(8) Lin, D.; Liu, Y.; Li, Y.; Li, Y.; Pei, A.; Xie, J.; Huang, W.; Cui, Y. Fast galvanic lithium corrosion involving a Kirkendall-type mechanism. *Nat. Chem.* **2019**, *11* (4), 382–389.

(9) Song, H.; Deng, H.; Li, C.; Feng, N.; He, P.; Zhou, H. Advances in lithium-containing anodes of aprotic Li-O₂ batteries: challenges and strategies for improvements. *Small Methods* **2017**, *1* (8), 1700135.

(10) Fang, R.; Zhao, S.; Sun, Z.; Wang, D. W.; Cheng, H. M.; Li, F. More reliable lithium-sulfur batteries: status, solutions and prospects. *Adv. Mater.* **2017**, *29* (48), 1606823.

(11) Wandt, J.; Marino, C.; Gasteiger, H. A.; Jakes, P.; Eichel, R.-A.; Granwehr, J. Operando electron paramagnetic resonance spectroscopy - formation of mossy lithium on lithium anodes during charge-discharge cycling. *Energy Environ. Sci.* **2015**, *8* (4), 1358–1367.

(12) Lin, D.; Liu, Y.; Cui, Y. Reviving the lithium metal anode for high-energy batteries. *Nat. Nanotechnol.* **2017**, *12* (3), 194–206.

(13) Han, F.; Westover, A. S.; Yue, J.; Fan, X.; Wang, F.; Chi, M.; Leonard, D. N.; Dudney, N. J.; Wang, H.; Wang, C. High electronic conductivity as the origin of lithium dendrite formation within solid electrolytes. *Nature Energy* **2019**, *4* (3), 187–196.

(14) Bai, P.; Li, J.; Brushett, F. R.; Bazant, M. Z. Transition of lithium growth mechanisms in liquid electrolytes. *Energy Environ. Sci.* **2016**, *9* (10), 3221–3229.

(15) Chang, H. J.; Illott, A. J.; Trease, N. M.; Mohammadi, M.; Jerschow, A.; Grey, C. P. Correlating microstructural lithium metal growth with electrolyte salt depletion in lithium batteries using 7Li MRI. *J. Am. Chem. Soc.* **2015**, *137* (48), 15209–16.

(16) Wang, X.; Zhang, M.; Alvarado, J.; Wang, S.; Sina, M.; Lu, B.; Bouwer, J.; Xu, W.; Xiao, J.; Zhang, J. G.; Liu, J.; Meng, Y. S. New insights on the structure of electrochemically deposited lithium metal and its solid electrolyte interphases via cryogenic TEM. *Nano Lett.* **2017**, *17* (12), 7606–7612.

(17) Peled, E.; Menkin, S. Review—SEI: past, present and future. *J. Electrochem. Soc.* **2017**, *164* (7), A1703–A1719.

(18) Zhi, J.; Yazdi, A. Z.; Valappil, G.; Haime, J.; Chen, P. Artificial solid electrolyte interphase for aqueous lithium energy storage systems. *Sci. Adv.* **2017**, *3* (9), No. e1701010.

(19) Yu, X.; Manthiram, A. Electrode-electrolyte interfaces in lithium-based batteries. *Energy Environ. Sci.* **2018**, *11* (3), 527–543.

(20) Li, W.; Yao, H.; Yan, K.; Zheng, G.; Liang, Z.; Chiang, Y. M.; Cui, Y. The synergistic effect of lithium polysulfide and lithium nitrate to prevent lithium dendrite growth. *Nat. Commun.* **2015**, *6*, 7436.

(21) Liang, X.; Wen, Z.; Liu, Y.; Wu, M.; Jin, J.; Zhang, H.; Wu, X. Improved cycling performances of lithium sulfur batteries with LiNO₃-modified electrolyte. *J. Power Sources* **2011**, *196* (22), 9839–9843.

(22) Lu, Y.; Tu, Z.; Archer, L. A. Stable lithium electrodeposition in liquid and nanoporous solid electrolytes. *Nat. Mater.* **2014**, *13* (10), 961–969.

(23) Qian, J.; Henderson, W. A.; Xu, W.; Bhattacharya, P.; Engelhard, M.; Borodin, O.; Zhang, J. G. High rate and stable cycling of lithium metal anode. *Nat. Commun.* **2015**, *6*, 6362.

(24) Fan, X.; Chen, L.; Ji, X.; Deng, T.; Hou, S.; Chen, J.; Zheng, J.; Wang, F.; Jiang, J.; Xu, K.; Wang, C. Highly fluorinated interphases enable high-voltage Li-metal batteries. *Chem.* **2018**, *4* (1), 174–185.

(25) Suo, L.; Xue, W.; Gobet, M.; Greenbaum, S. G.; Wang, C.; Chen, Y.; Yang, W.; Li, Y.; Li, J. Fluorine-donating electrolytes enable highly reversible 5-V-class Li metal batteries. *Proc. Natl. Acad. Sci. U. S. A.* **2018**, *115* (6), 1156–1161.

(26) Wang, C.; Meng, Y. S.; Xu, K. Perspective—Fluorinating Interphases. *J. Electrochem. Soc.* **2019**, *166* (3), A5184–A5186.

(27) Fan, X.; Chen, L.; Borodin, O.; Ji, X.; Chen, J.; Hou, S.; Deng, T.; Zheng, J.; Yang, C.; Liou, S. C.; Amine, K.; Xu, K.; Wang, C. Non-flammable electrolyte enables Li-metal batteries with aggressive cathode chemistries. *Nat. Nanotechnol.* **2018**, *13* (13), 715–722.

- (28) Albertus, P.; Babinec, S.; Litzelman, S.; Newman, A. Status and challenges in enabling the lithium metal electrode for high-energy and low-cost rechargeable batteries. *Nat. Energy* **2018**, *3* (1), 16–21.
- (29) Liu, S. F.; Wang, X. L.; Xie, D.; Xia, X. H.; Gu, C. D.; Wu, J. B.; Tu, J. P. Recent development in lithium metal anodes of liquid-state rechargeable batteries. *J. Alloys Compd.* **2018**, *730* (S), 135–149.
- (30) Zhang, Y. J.; Bai, W. Q.; Wang, X. L.; Xia, X. H.; Gu, C. D.; Tu, J. P. In situ confocal microscopic observation on inhibiting the dendrite formation of a-CN_x/Li electrode. *J. Mater. Chem. A* **2016**, *4*, 15597–15604.
- (31) Zheng, G.; Wang, C.; Pei, A.; Lopez, J.; Shi, F.; Chen, Z.; Sendek, A. D.; Lee, H.-W.; Lu, Z.; Schneider, H.; Safont-Sempere, M. M.; Chu, S.; Bao, Z.; Cui, Y. High-performance lithium metal negative electrode with a soft and flowable polymer coating. *ACS Energy Lett.* **2016**, *1* (6), 1247–1255.
- (32) Yan, K.; Lee, H. W.; Gao, T.; Zheng, G.; Yao, H.; Wang, H.; Lu, Z.; Zhou, Y.; Liang, Z.; Liu, Z.; Chu, S.; Cui, Y. Ultrathin two-dimensional atomic crystals as stable interfacial layer for improvement of lithium metal anode. *Nano Lett.* **2014**, *14* (10), 6016–22.
- (33) Steiger, J.; Kramer, D.; Mönig, R. Mechanisms of dendritic growth investigated by in situ light microscopy during electro-deposition and dissolution of lithium. *J. Power Sources* **2014**, *261*, 112–119.
- (34) Barai, P.; Higa, K.; Srinivasan, V. Effect of initial state of lithium on the propensity for dendrite formation: a theoretical study. *J. Electrochem. Soc.* **2017**, *164* (2), A180–A189.
- (35) Fan, X.; Ji, X.; Han, F.; Yue, J.; Chen, J.; Chen, L.; Deng, T.; Jiang, J.; Wang, C. Fluorinated solid electrolyte interphase enables highly reversible solid-state Li metal battery. *Sci. Adv.* **2018**, *4* (12), No. eaau9245.
- (36) Xu, R.; Han, F.; Ji, X.; Fan, X.; Tu, J.; Wang, C. Interface engineering of sulfide electrolytes for all-solid-state lithium batteries. *Nano Energy* **2018**, *53*, 958–966.
- (37) Zhao, J.; Liao, L.; Shi, F.; Lei, T.; Chen, G.; Pei, A.; Sun, J.; Yan, K.; Zhou, G.; Xie, J.; Liu, C.; Li, Y.; Liang, Z.; Bao, Z.; Cui, Y. Surface fluorination of reactive battery anode materials for enhanced stability. *J. Am. Chem. Soc.* **2017**, *139* (33), 11550–11558.
- (38) Zhang, X.-Q.; Cheng, X.-B.; Chen, X.; Yan, C.; Zhang, Q. Fluoroethylene carbonate additives to render uniform Li deposits in lithium metal batteries. *Adv. Funct. Mater.* **2017**, *27* (10), 1605989.
- (39) Ma, J. L.; Meng, F. L.; Yu, Y.; Liu, D. P.; Yan, J. M.; Zhang, Y.; Zhang, X. B.; Jiang, Q. Prevention of dendrite growth and volume expansion to give high-performance aprotic bimetallic Li-Na alloy-O₂ batteries. *Nat. Chem.* **2019**, *11* (1), 64–70.
- (40) Xue, L.; Gao, H.; Zhou, W.; Xin, S.; Park, K.; Li, Y.; Goodenough, J. B. Liquid K-Na alloy anode enables dendrite-free potassium batteries. *Adv. Mater.* **2016**, *28* (43), 9608–9612.
- (41) Li, X.; Liu, Y.; Pan, Y.; Wang, M.; Chen, J.; Xu, H.; Huang, Y.; Lau, W. M.; Shan, A.; Zheng, J.; Mitlin, D. A functional SrF₂ coated separator enabling a robust and dendrite-free solid electrolyte interphase on a lithium metal anode. *J. Mater. Chem. A* **2019**, *7* (37), 21349–21361.
- (42) Adams, B. D.; Zheng, J.; Ren, X.; Xu, W.; Zhang, J.-G. Accurate determination of Coulombic efficiency for lithium metal anodes and lithium metal batteries. *Adv. Energy Mater.* **2018**, *8* (7), 1702097.